

Dis-AE: Multi-domain & Multi-task Generalisation on Real-World Clinical Data

Daniel Kreuter^{1†}, Samuel Tull^{1†}, Julian Gilbey¹, Jacobus
Preller², BloodCounts! Consortium³, John A.D.
Aston⁴, James H.F. Rudd⁵, Suthesh
Sivapalaratnam⁶, Carola-Bibiane Schönlieb¹, Nicholas
Gleadall^{7,8} and Michael Roberts^{1*}

¹Department of Applied Mathematics and Theoretical Physics,
University of Cambridge, Wilberforce Road, Cambridge, CB3
0WA, United Kingdom.

²Addenbrooke's Hospital, Cambridge University Hospitals,
Cambridge, CB2 0QQ, United Kingdom.

³A list of authors and their affiliations appears at the end of the
paper.

⁴Department of Pure Mathematics and Mathematical Statistics,
University of Cambridge, Wilberforce Road, Cambridge, CB3
0WA, United Kingdom.

⁵Department of Medicine, University of Cambridge, Cambridge,
UK.

⁶Barts Health NHS Trust, London, UK.

⁷Department of Haematology, University of Cambridge,
Puddicombe Way, Cambridge Biomedical Campus, Cambridge,
CB2 0AW, United Kingdom.

⁸NHSBT, Long Road, Cambridge, CB2 0PT, United Kingdom.

*Corresponding author(s). E-mail(s): mr808@cam.ac.uk;

†These authors contributed equally to this work.

Abstract

Clinical data is often affected by clinically irrelevant factors such as discrepancies between measurement devices or differing processing methods between sites. In the field of machine learning (ML), these factors

are known as *domains* and the distribution differences they cause in the data are known as *domain shifts*. ML models trained using data from one domain often perform poorly when applied to data from another domain, potentially leading to wrong predictions. As such, developing machine learning models that can generalise well across multiple domains is a challenging yet essential task in the successful application of ML in clinical practice. In this paper, we propose a novel disentangled autoencoder (Dis-AE) neural network architecture that can learn domain-invariant data representations for multi-label classification of medical measurements even when the data is influenced by multiple interacting domain shifts at once. The model utilises adversarial training to produce data representations from which the domain can no longer be determined. We evaluate the model's domain generalisation capabilities on synthetic datasets and full blood count (FBC) data from blood donors as well as primary and secondary care patients, showing that Dis-AE improves model generalisation on multiple domains simultaneously while preserving clinically relevant information.

Keywords: Domain Generalisation, Full Blood Count, Domain Shift, Machine Learning

1 Introduction

Machine learning has promised to revolutionise healthcare for several years [1, 2]. Moreover, while there is an extensive literature describing high-performing machine learning models trained on immaculate benchmark datasets [3–5], such promising approaches rarely make it into clinical practice [6]. Often, this is because of an unexpected drop in performance when deploying the model on unseen test data due to *domain shift* [7, 8], i.e. there is a change in the data distribution between the dataset a model is trained on (*source* data) and that which it is deployed against (*target* data). Most common machine learning algorithms rely on an assumption that the source and target data are independent and identically distributed (i.i.d.) [9]. However, with domain shift, this assumption no longer holds, and model performance can be significantly affected. For medical datasets, domain shift is widespread, resulting from differences in equipment and clinical practice between sites [10–13], and models are vulnerable to associating clinically irrelevant features specific to the domain with their predictions, known as *shortcut learning* [14], which may lead to poor performance on target data.

For most medical applications, target data is rarely available prior to real-time deployment; thus, a *domain adaptation* approach, where pre-trained models are fine-tuned on data from the target distribution is not feasible. *Domain generalisation* techniques that focus on mitigating domain shift and improving model performance on unseen target data [15] are more practical

approaches. Various techniques have been developed in recent years: *data augmentation* [16, 17], where pre-processing is applied to source data in hopes of increasing data diversity; *domain alignment* [18, 19], where domain shift is minimised by appropriate feature transformations which re-align the data before model training, and *ensemble learning* [20–23], where an average of multiple models trained on different source distributions is taken. In medical datasets, particularly for tabular data, the extent and effect of unseen domains is often unknown, making alignment and augmentation impractical. For on-site deployment on non-specialised hardware, ensemble learning can often prove too expensive in terms of memory or computational time [24], particularly for deep neural network models.

Furthermore, in the sizeable domain generalisation literature, there is very little research into the problem of multiple interacting domains within any given dataset. In Figure 1, we indicate such a separation for some example domain shifts we observe in real-world datasets. Authors in the literature often refer to “domains” based solely on sample origin, rather than considering actual distribution-influencing effects causing domain shifts.

In this paper, we propose a deep learning model architecture based on feature disentanglement [25] to perform scalable domain generalisation for multiple interacting domains on tabular medical data. Such methods use multi-task learning to learn features useful for the desired task but penalise for learning features that can identify the sample’s domain label. Importantly, no prior knowledge of the expression of the domain shift is required. Our novel approach allows for multiple domains and tasks, both continuous and categorical, creating a truly disentangled embedding that can be used for multiple classification tasks. We test the model on both synthetic and real-life clinical datasets, with the goal of retaining high performance on data not used in training. The proposed architecture can be easily applied to other tabular data or images by adapting the corresponding model components.

Our novel contributions presented in this paper are:

- We introduce a domain-instance grouping that goes beyond the current domain generalisation literature by identifying and separating effects that cause domain shift in the data (e.g. Figure 1).
- We propose a novel disentangled autoencoder (Dis-AE) neural network model architecture to find a domain-agnostic lower-dimensional representation of the data. Dis-AE is easily scalable to multiple domains and classification tasks.
- We conduct experiments of Dis-AE, comparing it to a regular autoencoder on synthetic and real-life clinical data. We show that Dis-AE achieves high domain generalisation performance when using the same width and depth as the regular autoencoder.

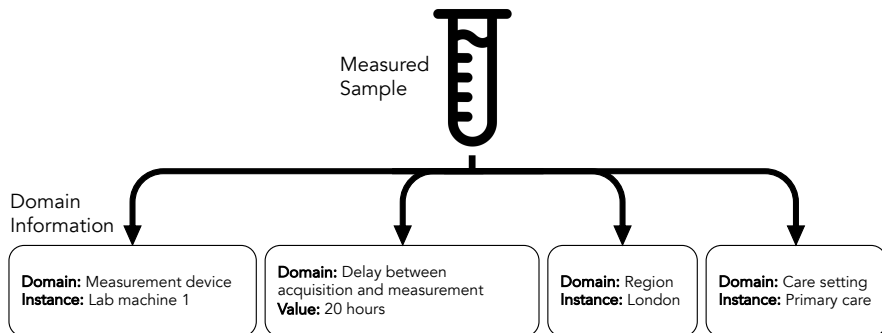


Fig. 1: Schematic displaying the proposed domain-instance grouping. As an example, labels for medical data are shown. Notably, domains can either be characterised by continuous values or be made up of categorical instances.

2 Materials & Methods

Datasets

We evaluate our model’s domain generalisation performance on four synthetic datasets, data from two clinical studies, and hospital patient data.

Synthetic datasets. The synthetic datasets **A**, **B**, and **C** represent a classification problem with increasing difficulty. Dataset A includes one task and one domain; dataset B adds multiple dependent continuous domains; dataset C adds two additional tasks (see Figure 2). The data was first generated using *scikit-learn*’s [26] `make_classification` (A, B) and `make_multilabel_classification` (C) functions. Afterwards, we added the artificial domains using simple transformations on some features of the data. Dataset A and Dataset B consist of 13 000 samples each, focusing on a single task with two balanced classes. Dataset C, on the other hand, comprises 26 000 samples involving three distinct tasks, each with two classes. While Task 2 maintains class balance, Task 1 and Task 3 exhibit imbalanced classes with a ratio of 5 : 2. To simulate domain shifts, we employed five affine instances in our datasets. These instances were created with a ratio of 5 : 5 : 1 : 1 : 1, ensuring that the majority of samples belong to the two instances used as source data. Additionally, other domain shifts in Dataset B and Dataset C were uniformly distributed across all samples.

To explore the generalisation limits of our model, we used the same procedure to make the **Many Affines** dataset, which includes a large number of instances on one domain and a single task. The dataset contains a large-scale collection of 500 000 samples, focusing on a single task with two balanced classes. Notably, these samples are evenly distributed among 70 distinct affine instances, offering a diverse range of transformation patterns for robust analysis.

The synthetic datasets and the applied domain transformations are summarised in Figure 2 (bottom) and Appendix A.

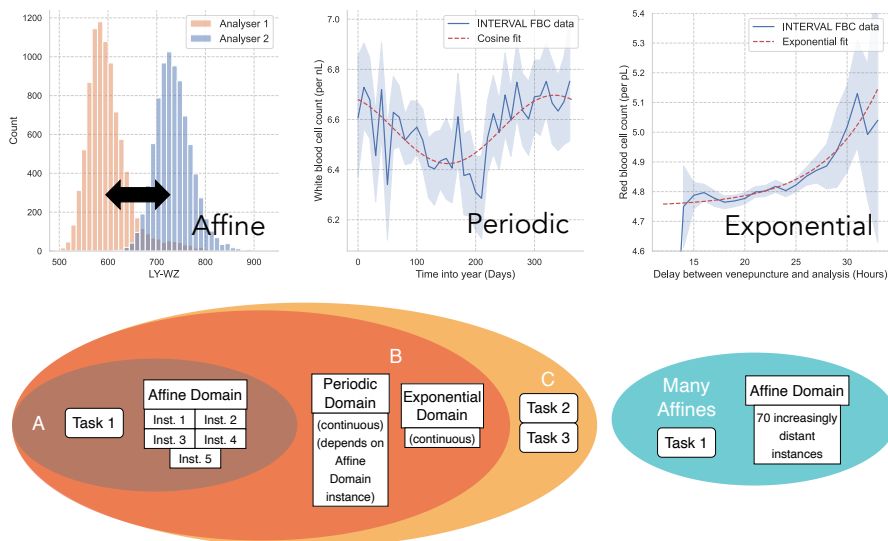


Fig. 2: Top: Examples of domain shifts found in real-world full blood count data from the INTERVAL trial. These shifts inspired the three transformations used in the synthetic datasets. (LY-WZ: Forward-scattered light distribution width of the LYMPH area on the white cell differential fluorescence scattergram. In the blue line plots, the line and shaded area show the mean and 95% confidence interval of the data.)

Bottom: Schematic describing the synthetic datasets and their task and domain properties.

Clinical datasets. We conduct experiments on multiple clinical datasets of haematological measurements. Specifically, we conduct experiments on features corresponding to standard high-level full blood count (HL-FBC) measurements, as well as further research and clustering parameters recorded by the haematology analyser machine during a full blood count. We refer to this data with additional features as *rich* full blood count (R-FBC) data. The parameters are described in Appendix B.

The datasets from **INTERVAL** [27] and **COMPARE** [28] contain R-FBC data from their respective clinical trials. These real-world datasets show natural domain shifts that occur when collecting R-FBC data in clinical practice (some shown in Figure 2). The studies collected samples from 48 460 and 29 029 donors, respectively. After pre-filtering (see Appendix C), we are left with 15 438 and 12 064 R-FBC samples, respectively. Sysmex XN-2000 haematology analysers were used for both blood donor studies, with two separate

machines used for INTERVAL’s analysis. The shift between analysers within the studies is strongly pronounced, as seen in Figure 2. Each measurement includes the times of both the donation appointment and the subsequent analysis in the corresponding haematology analyser. Additional information, such as the delay between venepuncture and measurement as well as the date of donation, can be determined from these times. Therefore, we consider the analyser, the delay between venepuncture and measurement, and time into the year (seasonal shifts) as our three domains of interest which result in a shift in the data but should not have an influence on our classification tasks. The analyser domain contains three instances since two Sysmex XN-2000 analysers were used in INTERVAL and one in COMPARE, while continuous time values represent the other two domains. As classification tasks, we selected subject sex, BMI bracket, and age bracket. While arguably lacking practical clinical value, we mainly chose these classification objectives to illustrate our proposed method’s performance and because they are clearly definable. The sample distributions for domains and tasks are displayed in Appendix C.

The dataset from **Cambridge University Hospitals (CUH)** [29] contains HL-FBC data from real-life clinical practice, including primary and secondary care data from 438 483 patients between 2016 and 2022. After pre-filtering (see Appendix D), we are left with 1 036 709 HL-FBC samples from 376 056 patients. The data at CUH was recorded on 5 ADVIA 2120 analysers which were gradually replaced with ADVIA 2120i machines throughout 2021 and 2022. Since one analyser at CUH is used exclusively for emergency cases, we chose to exclude all samples from the emergency 2120 and 2120i machines, leaving 8 analyser instances. Here too, the distribution difference between analysers is significant (Kolmogorov-Smirnoff test with statistic of 0.42 and p-value $\ll 0.001$ on RDW distributions). We again consider the previously mentioned delay between venepuncture and measurement and the time into the year as continuous domains. As classification tasks, we selected patient sex, age bracket, and care setting (i.e. whether they are treated in primary or secondary care). The sample distributions for domains and tasks are displayed in Appendix D.

Proposed Disentangled Autoencoder Model

We seek to achieve domain generalisation using a domain-adversarial learning approach. In such an approach, adversarial learning is used to find domain-agnostic features from which the source domain label of the data can no longer be predicted. We chose this method as we found it flexible, allowing for multiple domains and tasks. This framework also allows us to introduce an autoencoder architecture, thereby ensuring that the domain-agnostic learned embeddings of the data are also meaningful. Such embeddings cluster semantically similar inputs, making them valuable across various downstream models. Our proposed disentangled autoencoder (Dis-AE) model is largely inspired by Ganin & Lempitsky [25], who proposed a model for domain adaptation purposes. They trained an adversarial model where a feature extractor and a class label

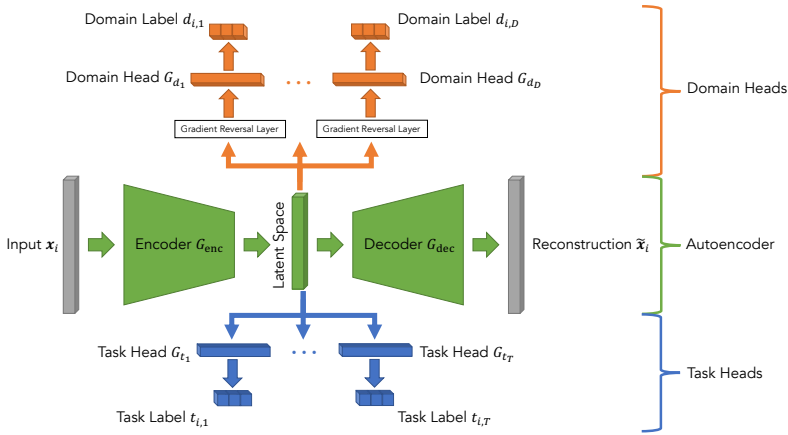


Fig. 3: The proposed disentangled autoencoder (Dis-AE) architecture includes an autoencoder as well as multiple task and domain heads attached to the autoencoder latent space. We train the model to maximise the performance of the task heads and decoder reconstruction while making the domain label prediction of the domain heads as difficult as possible. This adversarial training enables the model to learn a disentangled representation for multiple domains while ensuring good classification performance on multiple tasks.

predictor attempt to fool a domain classifier, reminiscent of other adversarial model concepts [30]. The key difference to other adversarial training schemes was the introduction of a *gradient reversal layer* which enables training all model parameters in one optimisation step rather than alternating between the adversarial parties. Trivedi et al. [31] later repurposed this general idea for domain generalisation for medical images to obtain disentangled image representations which do not contain image source information.

We extend this concept to tabular medical data and expand its capabilities in two major ways. Firstly, we incorporate a decoder network mirroring the feature extractor, to ensure the model learns to extract meaningful representations from the data. Secondly, we consider a more realistic separation when describing a dataset’s domain shift (see Figure 1) and introduce the option to add multiple *domain classifier heads* to the latent space of the model. Each domain head trains simultaneously and attempts to predict the corresponding domain label. Crucially, we allow for the classification of categorical or ordinal instance labels and regression to a continuous value label by discretising continuous domains into bins. We similarly propose adding multiple *task classifier heads* to the latent space, representing multiple classification tasks on the data. Figure 3 shows our proposed model architecture.

More formally, we consider our input space to be made up of N samples $\mathbf{x} \in X \subset \mathbb{R}^k$, which are one-dimensional vectors of tabular data with k features. We also assume that each sample \mathbf{x}_i has associated task labels $\{t_{i,1}, \dots, t_{i,T}\}$

and domain labels $\{d_{i,1}, \dots, d_{i,D}\}$, where T and D are the number of tasks and domains, respectively. *Tasks* are outcomes of interest (e.g. sample classification, patient illness) while *domains* are covariates of the data irrelevant to the tasks (see also Figure 1). We aim to obtain a domain-agnostic data representation. We assume, as is standard in the literature, that the data’s source and target distribution are similar but distinct and only differ by the domain shifts [15]. At training time, the model only has access to source domain distributions. We aim to train a model with high classification performance on the task labels and low autoencoder reconstruction error when given only samples from the target distribution.

For the proposed encoder G_{enc} , decoder G_{dec} architecture, with task heads $\{G_{t_j}\}$ and domain heads $\{G_{d_j}\}$, we consider the empirical error

$$\begin{aligned}
 E(\theta_{\text{enc}}, \theta_{\text{dec}}, \{\theta_t\}, \{\theta_d\}) &= \alpha \cdot \underbrace{\sum_{i=1}^N L_{\text{MSE}}(G_{\text{dec}}(G_{\text{enc}}(\mathbf{x}_i; \theta_{\text{enc}}); \theta_{\text{dec}}), \mathbf{x}_i)}_{\text{reconstruction loss}} \\
 &+ \beta \cdot \underbrace{\sum_{j=1}^T \sum_{i=1}^N L_{t_j}(G_{t_j}(G_{\text{enc}}(\mathbf{x}_i; \theta_{\text{enc}}); \theta_{t_j}), t_{i,j})}_{\text{task loss for task } j} \\
 &+ \underbrace{\sum_{j=1}^D \sum_{i=1}^N L_{d_j}(G_{d_j}(R_\lambda(G_{\text{enc}}(\mathbf{x}_i; \theta_{\text{enc}}))); \theta_{d_j}), d_{i,j})}_{\text{domain loss for domain } j} \\
 &\equiv \mathcal{L}_{\text{rec.}} + \mathcal{L}_{\text{task}} + \mathcal{L}_{\text{domain}}, \tag{1}
 \end{aligned}$$

where R_λ is the gradient reversal layer that is defined by the pseudo-function

$$R_\lambda(\mathbf{x}) = \mathbf{x} \tag{2}$$

$$\frac{dR_\lambda}{dx} = -\lambda \mathbf{I}, \tag{3}$$

where \mathbf{I} is the identity matrix [25]. The L_{t_j} and L_{d_j} terms represent the loss function of the j -th task and domain, respectively. For the classification objectives (i.e. task and domain labels), we use cross entropy loss with a softmax activation (we have not used ordinal losses in this work, though implementation would be trivial), while for autoencoder reconstruction, we use the mean-squared error loss L_{MSE} . The tuneable hyperparameters α , β , and λ control the importance of each of the three training objectives. We aim to find a saddle point of E such that

$$\hat{\theta}_{\text{enc}} = \arg \min_{\theta_{\text{enc}}} \mathcal{L}_{\text{rec.}} + \mathcal{L}_{\text{task}} - \mathcal{L}_{\text{domain}} \tag{4}$$

$$\hat{\theta}_{\text{dec}} = \arg \min_{\theta_{\text{dec}}} \mathcal{L}_{\text{rec}}. \quad (5)$$

$$\{\hat{\theta}_t\} = \arg \min_{\{\theta_t\}} \mathcal{L}_{\text{task}} \quad (6)$$

$$\{\hat{\theta}_d\} = \arg \min_{\{\theta_d\}} \mathcal{L}_{\text{domain}}. \quad (7)$$

The inclusion of gradient reversal layers allows running gradient descent-based minimisation on $\mathcal{L}_{\text{rec.}} + \mathcal{L}_{\text{task}} + \mathcal{L}_{\text{domain}}$ with respect to all parameters $(\theta_{\text{enc}}, \theta_{\text{dec}}, \{\theta_t\}, \{\theta_d\})$ at once to find the optimal parameters (4)–(7) [25].

Out-of-Distribution Evaluation

Ye et al. [32] developed a theoretical framework on what it means for an out-of-distribution (OOD) problem to be *learnable* by a model. We adapt their model selection method and use their definition of model variation as a baseline for our reliability assessment.

Measuring Disentanglement

For a feature $\phi(\mathbf{x})$ in the latent space generated by $G_{\text{enc}}(\mathbf{x})$ and a dataset with domain and task labels as described above, the *variation* of feature ϕ for task τ across domain δ is given by

$$\mathcal{V}(\phi, \tau, \delta) := \max_{(y, e, e') \in \{t_\tau\} \times \{d_\delta\} \times \{d_\delta\}} \rho \left(P(\phi^e | y), P(\phi^{e'} | y) \right), \quad (8)$$

where ϕ^e is the latent feature ϕ of all data with label e for domain δ , $\rho(P, Q)$ is a symmetric function with which we measure dissimilarity between distributions P and Q , and $\{t_\tau\}$ and $\{d_\delta\}$ are the unique labels of task τ and domain δ , respectively. For the purpose of model selection, we use the 1-dimensional Wasserstein-2 (ρ_{W_2}) metric, implemented in the Python Optimal Transport (POT) [33] package,

$$\rho_{W_2}(P, Q) = \sqrt{\min_{\gamma \in \mathbb{R}_+^{m \times n}} \sum_{i,j} \gamma_{ij} (x_i - y_j)^2} \quad (9)$$

$$\text{s.t. } \gamma \mathbf{I} = P; \gamma^\top \mathbf{I} = Q; \gamma \geq 0, \quad (10)$$

where $x \in P$, $y \in Q$ and m and n are the number of data points in P and Q , respectively. We use ρ_{W_2} for this task since it monotonically increases with the distance between distributions. In contrast, other metrics such as the total variation distance saturate as soon as the distributions no longer overlap. Due to the use of this metric in hyperparameter tuning, a continuous dependence on the distance between distributions is desirable. Overall, $\mathcal{V}_\rho(\phi, t, d)$ describes the variation of a feature in the latent space across a domain. Hence, \mathcal{V} should be small in a disentangled representation. Due to various scales within features,

in practice, we first normalise the feature distribution to zero-mean and unit standard deviation, and then calculate $\rho\left(P(\phi^e|y), P(\phi^{e'}|y)\right)$.

Since Ye et al. [32] only consider one task and domain, we define feature variation across all tasks and domains as

$$V(\phi) := \max_{\substack{\tau \in \{1, \dots, T\} \\ \delta \in \{1, \dots, D\}}} \mathcal{V}(\phi, \tau, \delta). \quad (11)$$

To get a measure of the variation over the full latent space, we use the *model variation* of the encoder:

$$V^{\text{sup}}(G_{\text{enc}}) := \sup_{u \in \mathcal{S}^{m-1}} V(u^\top G_{\text{enc}}(\mathbf{X})), \quad (12)$$

where $G_{\text{enc}}(\mathbf{X})$ is the list of latent space representations of all $\mathbf{x} \in \mathbf{X}$, m is the latent space dimension, and \mathcal{S}^{m-1} is the unit $(m-1)$ -sphere, and therefore $u^\top G_{\text{enc}}(\mathbf{X})$ is a vector. We can use $V^{\text{sup}}(G_{\text{enc}})$ as an intuitive measure of how much the latent space varies across source domains. This allows us to measure how successfully domains have been disentangled.

Model Selection Score

To select the best-performing model hyperparameters, we required a combined measure of how well a model performs on all three training objectives (reconstruction, task classification, domain disentanglement). Ye et al. [32] suggest a score comprised of a model's classification performance and its variation as a metric for model selection. Since we additionally aim for good reconstruction performance, our proposed **Selection Score** for a model f instead consists of three terms:

$$\text{Score}(f) := \underbrace{\frac{1}{T} \sum_{\tau \in \{1, \dots, T\}} \text{Acc}_{\tau, f}}_{\text{mean task accuracy}} - \underbrace{\frac{V^{\text{sup}}(G_{\text{enc}, f})}{V^{\text{sup}}(\mathbf{I})}}_{\text{rel. model variation}} - \underbrace{\sqrt{\frac{\text{MSE}(\mathbf{X}, \tilde{\mathbf{X}})}{\mathbb{E}(\mathbf{X}^2)}}}_{\text{rel. rec. error}}, \quad (13)$$

where $\text{MSE}(\mathbf{X}, \tilde{\mathbf{X}})$ is the mean-squared error between input data \mathbf{X} and its reconstruction $\tilde{\mathbf{X}}$ by the model and $\mathbb{E}(\mathbf{X}^2)$ is the mean of all squared samples $\|\mathbf{x}\|_2^2$. $V^{\text{sup}}(\mathbf{I})$ gives the domain variation of the data without any embedding transformation.

Since the second and third terms in Eq. (13) are unbounded (depending on choice of ρ), $\text{Score}(f) \in (-\infty, 1]$, where a score close to 1 is desirable.

Reliability Assessment

The variation of a model, as defined in Eq. (12), can be used to quantify the dissimilarity between domains for any dataset, whether it is in full-dimensional

space or a lower-dimensional embedding space. A successful domain generalisation model should maintain similar model variation on source and target data. For reliability assessment experiments, we used the Jensen-Shannon divergence

$$\rho_{\text{JSD}}(P, Q) = \frac{1}{2}D(P, M) + \frac{1}{2}D(Q, M), \quad (14)$$

instead of the Wasserstein distance in the calculation of V^{sup} . Here, $D(P, Q)$ is the Kullback-Leibler divergence [34] and $M = \frac{1}{2}(P + Q)$. This was chosen as $\rho_{\text{JSD}}(P, Q)$ is the reduction in uncertainty of a random variable X , given knowledge of whether it originated from P or Q (mutual information [34]). Using the Jensen-Shannon divergence in the calculation of V^{sup} is thus a direct measurement of how much domain information is contained within our data representation. For V^{sup} close to 0, there is no domain shift; for V^{sup} close to 1, the distributions are completely separated.

Architecture Selection for Dis-AE

The Dis-AE architecture may be viewed as a “vanilla” autoencoder (AE) with task and domain heads. Therefore, to determine an optimal Dis-AE architecture, we begin by identifying the best AE structure. In all experiments, we perform hyperparameter tuning on a vanilla AE with fully-connected layers to optimise the network’s depth and width. We then optimise the hyperparameters of the Dis-AE model with respect to the selection score from Eq. (13), while keeping the network architecture (i.e., depth and width) the same as the vanilla AE. The AE consists of fully-connected linear layers, ReLU activations, and a learning rate scheduler that reduces the learning rate when the validation loss reaches a plateau. We perform hyperparameter tuning of the Dis-AE model for the α , β , and λ parameters (see Eq. (1)) and an L2-regularisation parameter. We perform hyperparameter tuning using the Weights and Biases [35] framework and the Cambridge Service for Data-Driven Discovery (CSD3) high-performance computing platform, exhaustively searching among parameter combinations.

Throughout this work, all reported experimental results were obtained as the average of a 5-fold cross-validation experiment. Additionally, we trained the models 5 times per fold and selected the best performing models for each fold. This was done to mitigate differences due to weight initialisation.

3 Results

Performance of the Proposed Model

Data	Model	Acc. Term	Var. Term	Rec. Term	Score
Data A	Vanilla AE	0.97	1.011	0.05	-0.09
	Dis-AE	0.98	0.003	0.08	0.89
Data B	Vanilla AE	0.96	0.693	0.06	0.21
	Dis-AE	0.98	0.011	0.17	0.80
Data C	Vanilla AE	{0.77, 0.73, 0.71}	0.633	0.24	-0.14
	Dis-AE	{0.81, 0.77, 0.73}	0.074	0.37	0.33
INTERVAL	Vanilla AE	{0.85, 0.28, 0.51}	1.993	0.16	-1.61
	Dis-AE	{0.85, 0.28, 0.50}	0.219	0.21	0.11
CUH	Vanilla AE	{0.75, 0.24, 0.77}	1.089	0.02	-0.52
	Dis-AE	{0.75, 0.24, 0.74}	0.631	0.14	-0.19

Table 1: Task classification accuracy, relative model variation, and relative reconstruction error, combined to give selection score (Eq. (13)). The results were obtained from experiments on various datasets using a vanilla AE and the Dis-AE model. For the synthetic datasets, instances 1&2 of domain 1 were selected as source data (see Section 2). For multi-task problems, the accuracy per task is displayed. The tasks for the INTERVAL dataset are subject {sex, age bracket, and BMI bracket}. For the CUH dataset, the two analysers with the highest variation HL-FBC data were selected as source data. The tasks for the CUH dataset are patient {sex, age bracket, and care setting}. During training, we used weighted random sampling to create batches with balanced care setting numbers.

The selection score given in Eq. (13) (and its constituent terms) give an illustrative metric of the model’s performance. Table 1 displays these terms for both the vanilla AE and Dis-AE models for all datasets. Further experimental results, including task classification accuracies for the various datasets, are included in Appendix E, where we see similar behaviour. An illustration of generalisation performance is given by Table 2, where domain generalisation performance on INTERVAL (source) and COMPARE (target) data is displayed using the model variation (Eq. 12).

Figure 4 displays *Potential of Heat diffusion for Affinity-based Transition Embedding* (PHATE) [36] visualisations of the three representations of the rich FBC data of the INTERVAL and COMPARE studies. We trained the Dis-AE model on three tasks: subject sex, age, and BMI; and three domains: haematology analyser, the delay between venepuncture and analysis, and time of year.

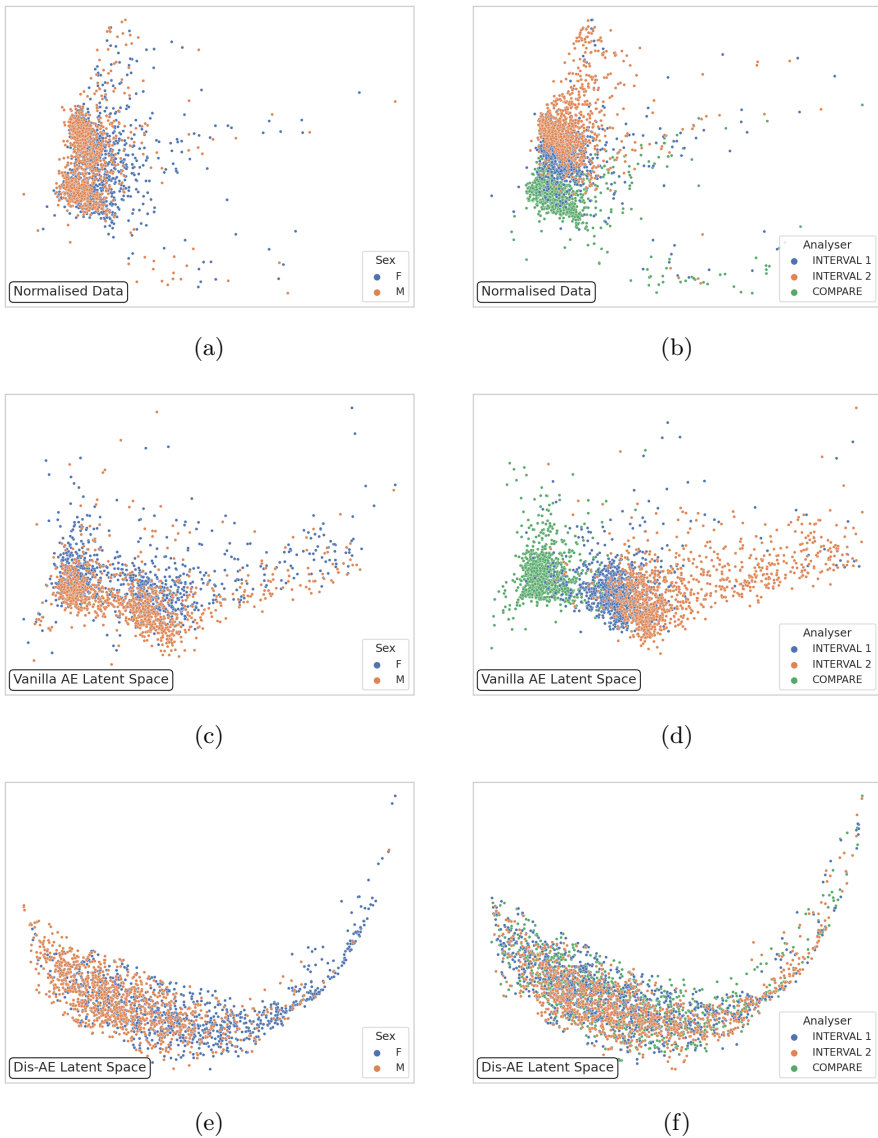


Fig. 4: Rich FBC donor data PHATE [36] visualisation of normalised raw data (row 1) and latent spaces of a vanilla AE (row 2) and the Dis-AE model (row 3). The images in the left column are coloured by subject sex (example task), while those in the right column are coloured by haematology analyser (example domain). The machine learning models were only trained on data from INTERVAL.

Representation	Domain	Variation V^{sup}	
		Within source (INTERVAL)	Source and target (INT \cup COM)
(A) Raw data	Analysers	0.50	0.89
	Sample age	0.90	0.86
	Time of year	0.77	0.91
(B) Vanilla AE	Analysers	0.46	0.67
	Sample age	0.84	0.83
	Time of year	0.62	0.85
(C) Dis-AE	Analysers	0.24	0.31
	Sample age	0.59	0.61
	Time of year	0.66	0.74

Table 2: Variation of rich FBC data from the INTERVAL and COMPARE studies in different representations. The three representations are: (A) the unmodified data, (B) the latent space of a vanilla AE and (C) the latent space of the Dis-AE model. The variation V^{sup} , calculated using ρ_{JSD} , is shown per domain to show each covariate’s contribution to the data’s domain shift.

Robustness Evaluation

We want to understand the extent to which the target data distribution can differ from the source distributions while preserving model robustness. To this end, we trained a vanilla AE and the Dis-AE model multiple times, varying the number of instances included in the source data to evaluate the robustness on the target data, using the Many Affines dataset. Figure 5 shows both models' variation V^{sup} on increasingly distant target data and classification accuracy on the synthetic task.

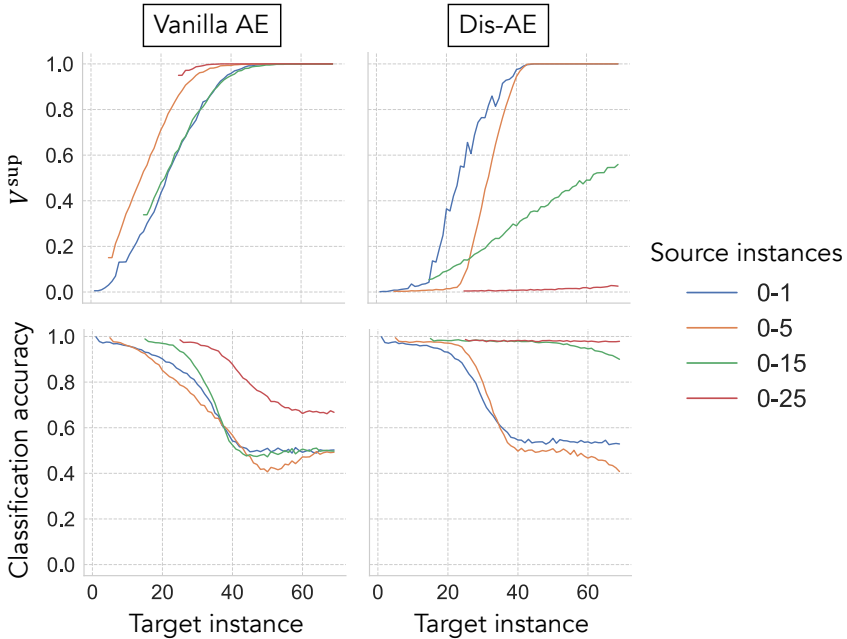


Fig. 5: Results of evaluating vanilla AE and Dis-AE model performance for a dataset with many instances with affine domain shift. The diversity and size of the source dataset were varied for different runs to investigate the effect on target data generalisation. The quantities shown are V^{sup} using ρ_{JSD} (Eq. (14)) and the task accuracy.

As mentioned in Section 2, we used the Jensen-Shannon divergence to calculate V^{sup} to measure mutual information between the latent space representations of the data and the source and target distributions. From the right column in Figure 5, it is visible that training the Dis-AE model on more diverse source data results in a slower decay in task and generalisation performance. A vanilla AE does not reflect this behaviour (left column in Figure 5).

4 Discussion

Our goal was to develop an approach to obtain lower-dimensional data representations that preserve informative features for outcomes of interest while eliminating influences on the data known to be irrelevant covariates. This approach could be used in a medical setting, for example, to retain clinically relevant features within the data representation while ignoring irrelevant ones, enabling training of classifiers which generalise across multiple domains. We proposed the disentangled autoencoder (Dis-AE) model as this approach and used the proposed model selection score from Eq. (13) to illustrate its performance. Table 1 displays the results, with the accuracy term representing the model's ability to maintain informative features within its latent space. The task performance is comparable to that of a vanilla AE. However, as supported by the results in the model variation term, Dis-AE can maintain high task performance while drastically reducing domain shift within its representation space. This improvement over a classical embedding model (vanilla AE) and the raw data is also evident from the PHATE visualisations in Figure 4. Additionally, Table 2 demonstrates Dis-AE's ability to maintain low model variation in the latent space on unseen data, even when the variation increases on the raw data.

We investigated the Dis-AE model's OOD robustness by measuring its performance on increasingly distant OOD target data. As seen in Figure 5, Dis-AE maintains high task and generalisation performance even on highly OOD data, given enough diversity in the source data. This behaviour strongly suggests that using data from multiple sources can significantly increase model robustness in a real-world deployment setting.

Dis-AE stands out from current domain generalisation approaches as it, for the first time, considers multiple domains and tasks within its design and, as such, can separate multiple independent domain shift influences on the data. Dis-AE is scalable to many domains and tasks and can be easily modified by adding or removing classifier heads from its latent space. Including the gradient reversal layer ensures fast convergence, enabling single-step updates to all model parameters. The Dis-AE framework can be adapted to other model architectures by modifying the autoencoder part of the model to include, e.g. convolutional layers or skip-connections. Dis-AE will open up future research on data where domain shift is expected to be caused by many domains and where the exact nature of the shift is unknown. In particular, it allows for joint data embeddings where the data originated from multiple sources.

The proposed model has several limitations. As seen in Table 1, Dis-AE's reconstruction quality is lower than that of a vanilla AE due to conflicting objectives: removing domain information from the latent space while preserving it in the reconstruction. To overcome this, future work could involve providing the decoder with explicit domain labels, such that the decoder can rely on this additional information alongside the latent space to produce accurate reconstructions of the input data. Additionally, Dis-AE training proved somewhat unstable, converging to unsatisfactory results around 20% of the

time. Adversarial training schemes, like the one used, are notoriously unstable [37, 38]. Improving convergence reliability will require further research. Fortunately, in our experiments, model training consistently completed within 10 minutes on a modern laptop, minimising concerns about re-training.

5 Conclusion

In this paper, we propose a novel model architecture for domain generalisation, namely a disentangled autoencoder (Dis-AE). Unlike previous work, we propose a new hierarchy for domain shift problems where we consider domains as distinct covariates which cause a shift in the data. Domains can either be characterised by continuous values (e.g. time) or consist of categorical instances (e.g. measurement device). The Dis-AE framework includes a gradient reversal layer for fast convergence and is easily adaptable to other model architectures. We compare the performance of Dis-AE to a “vanilla” autoencoder on multiple synthetic datasets and real-life clinical data. The results of the experiments demonstrate the significantly increased generalisation performance of our model and provide evidence that the Dis-AE design encourages increased model robustness when trained on more diverse training data.

Dis-AE provides a scalable solution for future research on large collaborative medical datasets suffering from domain shift on many domains. This may be particularly useful in multi-centre studies and trials using repeated measurements.

Code availability

The code is publicly available at [inserted on acceptance].

Availability of data and materials

The synthetic datasets are available in the above GitLab repository. The INTERVAL and COMPARE datasets are both available from the respective study teams on reasonable request. The Epicov dataset is a private dataset held by Cambridge University Hospitals NHS Trust and is not available publicly.

References

- [1] Sadegh-Zadeh, K.: In dubio pro aegro. *Artificial Intelligence in Medicine* **2**(1), 1–3 (1990). [https://doi.org/10.1016/0933-3657\(90\)90012-G](https://doi.org/10.1016/0933-3657(90)90012-G)
- [2] Handelman, G.S., Kok, H.K., Chandra, R.V., Razavi, A.H., Lee, M.J., Asadi, H.: eDoctor: Machine learning and the future of medicine. *Journal of Internal Medicine* **284**(6), 603–619 (2018). <https://doi.org/10.1111/joim.12822>
- [3] Milletari, F., Navab, N., Ahmadi, S.-A.: V-Net: Fully Convolutional Neural Networks for Volumetric Medical Image Segmentation. In: 2016 Fourth International Conference on 3D Vision (3DV), pp. 565–571 (2016). <https://doi.org/10.1109/3DV.2016.79>
- [4] Han, C., Rundo, L., Murao, K., Noguchi, T., Shimahara, Y., Milacski, Z.Á., Koshino, S., Sala, E., Nakayama, H., Satoh, S.: MADGAN: Unsupervised medical anomaly detection GAN using multiple adjacent brain MRI slice reconstruction. *BMC Bioinformatics* **22**(2), 31 (2021). <https://doi.org/10.1186/s12859-020-03936-1>
- [5] Cao, H., Wang, Y., Chen, J., Jiang, D., Zhang, X., Tian, Q., Wang, M.: Swin-Unet: Unet-like Pure Transformer for Medical Image Segmentation. *arXiv* (2021). <https://doi.org/10.48550/arXiv.2105.05537>
- [6] Teodoridis, F., Goldfarb, A.: Why Is AI Adoption in Health Care Lagging? (2022)
- [7] Recht, B., Roelofs, R., Schmidt, L., Shankar, V.: Do ImageNet Classifiers Generalize to ImageNet? In: *Proceedings of the 36th International Conference on Machine Learning*, pp. 5389–5400. PMLR, ??? (2019)
- [8] Moreno-Torres, J.G., Raeder, T., Alaiz-Rodríguez, R., Chawla, N.V., Herrera, F.: A unifying view on dataset shift in classification. *Pattern Recognition* **45**(1), 521–530 (2012). <https://doi.org/10.1016/j.patcog.2011.06.019>
- [9] Bishop, C.M.: *Pattern Recognition and Machine Learning*. Information Science and Statistics. Springer, New York (2006)
- [10] Liu, X., Thermos, S., O’Neil, A., Tsaftaris, S.A.: Semi-Supervised Meta-learning with Disentanglement for Domain-generalised Medical Image Segmentation (2021). <https://doi.org/10.48550/arXiv.2106.13292>
- [11] Tao, Q., Yan, W., Wang, Y., Paiman, E.H.M., Shamonin, D.P., Garg, P., Plein, S., Huang, L., Xia, L., Sramko, M., Tintera, J., de Roos, A., Lamb, H.J., van der Geest, R.J.: Deep Learning-based Method for

- Fully Automatic Quantification of Left Ventricle Function from Cine MR Images: A Multivendor, Multicenter Study. *Radiology* **290**(1), 81–88 (2019). <https://doi.org/10.1148/radiol.2018180513>
- [12] Thiagarajan, J.J., Rajan, D., Sattigeri, P.: Understanding Behavior of Clinical Models under Domain Shifts. *arXiv* (2019). <https://doi.org/10.48550/arXiv.1809.07806>
- [13] Roland, T., Böck, C., Tschoellitsch, T., Maletzky, A., Hochreiter, S., Meier, J., Klambauer, G.: Domain Shifts in Machine Learning Based Covid-19 Diagnosis From Blood Tests. *Journal of Medical Systems* **46**(5), 23 (2022). <https://doi.org/10.1007/s10916-022-01807-1>
- [14] Geirhos, R., Jacobsen, J.-H., Michaelis, C., Zemel, R., Brendel, W., Bethge, M., Wichmann, F.A.: Shortcut Learning in Deep Neural Networks. *Nature Machine Intelligence* **2**(11), 665–673 (2020) <https://arxiv.org/abs/2004.07780> [cs, q-bio]. <https://doi.org/10.1038/s42256-020-00257-z>
- [15] Zhou, K., Liu, Z., Qiao, Y., Xiang, T., Loy, C.C.: Domain Generalization: A Survey. *IEEE Transactions on Pattern Analysis and Machine Intelligence*, 1–20 (2022). <https://doi.org/10.1109/TPAMI.2022.3195549>
- [16] Otálora, S., Atzori, M., Andrearczyk, V., Khan, A., Müller, H.: Staining Invariant Features for Improving Generalization of Deep Convolutional Neural Networks in Computational Pathology. *Frontiers in Bioengineering and Biotechnology* **7** (2019)
- [17] Zhou, K., Yang, Y., Hospedales, T., Xiang, T.: Learning to Generate Novel Domains for Domain Generalization. In: Vedaldi, A., Bischof, H., Brox, T., Frahm, J.-M. (eds.) *Computer Vision – ECCV 2020. Lecture Notes in Computer Science*, pp. 561–578. Springer International Publishing, Cham (2020). https://doi.org/10.1007/978-3-030-58517-4_33
- [18] Li, H., Wang, Y., Wan, R., Wang, S., Li, T.-Q., Kot, A.: Domain Generalization for Medical Imaging Classification with Linear-Dependency Regularization. In: *Advances in Neural Information Processing Systems*, vol. 33, pp. 3118–3129. Curran Associates, Inc., ??? (2020)
- [19] Hu, S., Zhang, K., Chen, Z., Chan, L.: Domain Generalization via Multidomain Discriminant Analysis. In: *Proceedings of The 35th Uncertainty in Artificial Intelligence Conference*, pp. 292–302. PMLR, ??? (2020)
- [20] Ding, Z., Fu, Y.: Deep Domain Generalization With Structured Low-Rank Constraint. *IEEE Transactions on Image Processing* **27**(1), 304–313 (2018). <https://doi.org/10.1109/TIP.2017.2758199>

- [21] Xu, Z., Li, W., Niu, L., Xu, D.: Exploiting Low-Rank Structure from Latent Domains for Domain Generalization. In: Fleet, D., Pajdla, T., Schiele, B., Tuytelaars, T. (eds.) *Computer Vision – ECCV 2014. Lecture Notes in Computer Science*, pp. 628–643. Springer International Publishing, Cham (2014). https://doi.org/10.1007/978-3-319-10578-9_41
- [22] Wang, S., Yu, L., Li, K., Yang, X., Fu, C.-W., Heng, P.-A.: DoFE: Domain-Oriented Feature Embedding for Generalizable Fundus Image Segmentation on Unseen Datasets. *IEEE Transactions on Medical Imaging* **39**(12), 4237–4248 (2020). <https://doi.org/10.1109/TMI.2020.3015224>
- [23] Nozza, D., Fersini, E., Messina, E.: Deep Learning and Ensemble Methods for Domain Adaptation. In: 2016 IEEE 28th International Conference on Tools with Artificial Intelligence (ICTAI), pp. 184–189 (2016). <https://doi.org/10.1109/ICTAI.2016.0037>
- [24] Bifet, A., Holmes, G., Pfahringer, B., Kirkby, R., Gavaldà, R.: New ensemble methods for evolving data streams. In: *Proceedings of the 15th ACM SIGKDD International Conference on Knowledge Discovery and Data Mining. KDD '09*, pp. 139–148. Association for Computing Machinery, New York, NY, USA (2009). <https://doi.org/10.1145/1557019.1557041>
- [25] Ganin, Y., Lempitsky, V.: Unsupervised domain adaptation by back-propagation. In: Bach, F., Blei, D. (eds.) *Proceedings of the 32nd International Conference on Machine Learning. Proceedings of Machine Learning Research*, vol. 37, pp. 1180–1189. PMLR, Lille, France (2015)
- [26] Pedregosa, F., Varoquaux, G., Gramfort, A., Michel, V., Thirion, B., Grisel, O., Blondel, M., Prettenhofer, P., Weiss, R., Dubourg, V., Vanderplas, J., Passos, A., Cournapeau, D., Brucher, M., Perrot, M., Duchesnay, E.: Scikit-learn: Machine learning in Python. *Journal of Machine Learning Research* **12**, 2825–2830 (2011)
- [27] Angelantonio, E.D., Thompson, S.G., Kaptoge, S., Moore, C., Walker, M., Armitage, J., Ouwehand, W.H., Roberts, D.J., Danesh, J., Angelantonio, E.D., Thompson, S.G., Kaptoge, S., Moore, C., Walker, M., Armitage, J., Ouwehand, W.H., Roberts, D.J., Danesh, J., Armitage, J., Danesh, J., Angelantonio, E.D., Donovan, J., Ford, I., Henry, R., Hunt, B.J., Huray, B.L., Mehenny, S., Mifflin, G., Moore, C., Ouwehand, W.H., Green, J., Roberts, D.J., Stredder, M., Thompson, S.G., Walker, M., Watkins, N.A., McDermott, A., Ronaldson, C., Thomson, C., Tolkien, Z., Williamson, L., Allen, D., Danesh, J., Angelantonio, E.D., Henry, R., Mehenny, S., Moore, C., Ouwehand, W.H., Roberts, D.J., Sambrook, J., Walker, M., Hammerton, T., Thomson, C., Tolkien, Z., Allen, D., Bruce, D., Choudry, F., Angelantonio, E.D., Ghevaert, C., Johnston, K., Kelly, A., King, A., Mehenny, S., Mifflin, G., Mo, A., Moore, C., Ouwehand,

- W.H., Page, L., Richardson, P., Roberts, D.J., Sambrook, J., Senior, P., Umrana, Y., Walker, M., Wong, H., Kaptoge, S., Murphy, G., Newland, A.C., Wheatley, K., Greaves, M., Turner, M., Aziz, T., Brain, R., Davies, C., Turner, R., Wakeman, P., Dent, A., Wakeman, A., Anthony, B., Bland, D., Parrondo, W., Vincent, H., Weatherill, C., Forsyth, A., Butterfield, C., Wright, T., Ellis, K., Johnston, K., Poynton, P., Brooks, C., Martin, E., Littler, L., Williams, L., Blair, D., Ackerley, K., Woods, L., Stanley, S., Walsh, G., Franklin, G., Howath, C., Sharpe, S., Smith, D., Botham, L., Williams, C., Alexander, C., Sowerbutts, G., Furnival, D., Thake, M., Patel, S., Roost, C., Sowerby, S., Appleton, M.J., Bays, E., Bowyer, G., Clarkson, S., Halson, S., Holmes, K., Humphries, G., Johnston, K., Parvin-Cooper, L., Towler, J., Addy, J., Barrass, P., Stennett, L., Burton, S., Dingwall, H., Henry, R., Clarke, V., Potton, M., Thomson, C., Bolton, T., Daynes, M., Halson, S., Spackman, S., Walker, M., Momodu, A., Fenton, J., King, A., Muhammed, O., Oates, N., Peakman, T., Ryan, C., Spreckley, K., Stubbins, C., Williams, J., Brennan, J., Mochon, C., Taylor, S., Warren, K., Kaptoge, S., Thompson, S.G., Angelantonio, E.D., Moore, C., Mant, J., Ouweland, W.H., Thompson, S.G., Danesh, J., Roberts, D.J.: Efficiency and safety of varying the frequency of whole blood donation (INTERVAL): A randomised trial of 45 000 donors. *The Lancet* **390**(10110), 2360–2371 (2017). [https://doi.org/10.1016/s0140-6736\(17\)31928-1](https://doi.org/10.1016/s0140-6736(17)31928-1)
- [28] Bell, S., Sweeting, M., Ramond, A., Chung, R., Kaptoge, S., Walker, M., Bolton, T., Sambrook, J., Moore, C., McMahon, A., Fahle, S., Cullen, D., Mehenny, S., Wood, A.M., Armitage, J., Ouweland, W.H., Mifflin, G., Roberts, D.J., Danesh, J., and, E.D.A.: Comparison of four methods to measure haemoglobin concentrations in whole blood donors (COMPARE): A diagnostic accuracy study. *Transfusion Medicine* **31**(2), 94–103 (2020). <https://doi.org/10.1111/tme.12750>
- [29] EpiCov Version1.0. <https://www.hra.nhs.uk/planning-and-improving-research/application-summaries/research-summaries/epicov-version10/>
- [30] Goodfellow, I., Pouget-Abadie, J., Mirza, M., Xu, B., Warde-Farley, D., Ozair, S., Courville, A., Bengio, Y.: Generative adversarial networks. *Communications of the ACM* **63**(11), 139–144 (2020). <https://doi.org/10.1145/3422622>
- [31] Trivedi, A., Robinson, C., Blazes, M., Ortiz, A., Desbiens, J., Gupta, S., Dodhia, R., Bhatraju, P.K., Liles, W.C., Kalpathy-Cramer, J., Lee, A.Y., Ferrer, J.M.L.: Deep learning models for COVID-19 chest x-ray classification: Preventing shortcut learning using feature disentanglement. *PLOS ONE* **17**(10), 0274098 (2022). <https://doi.org/10.1371/journal.pone.0274098>

- [32] Ye, H., Xie, C., Cai, T., Li, R., Li, Z., Wang, L.: Towards a Theoretical Framework of Out-of-Distribution Generalization. In: *Advances in Neural Information Processing Systems*, vol. 34, pp. 23519–23531. Curran Associates, Inc., ??? (2021)
- [33] Flamary, R., Courty, N., Gramfort, A., Alaya, M.Z., Boisbunon, A., Chambon, S., Chapel, L., Corenflos, A., Fatras, K., Fournier, N., Gautheron, L., Gayraud, N.T.H., Janati, H., Rakotomamonjy, A., Redko, I., Rolet, A., Schutz, A., Seguy, V., Sutherland, D.J., Tavenard, R., Tong, A., Vayer, T.: POT: Python optimal transport. *Journal of Machine Learning Research* **22**(78), 1–8 (2021)
- [34] Cover, T.M.: Elements of information theory thomas M. Cover, joy A. Thomas. In: *Elements of Information Theory*, 2nd ed. edn. Wiley-Interscience, Hoboken, N.J. (2006)
- [35] Biewald, L.: *Experiment Tracking with Weights and Biases* (2020)
- [36] Moon, K.R., van Dijk, D., Wang, Z., Gigante, S., Burkhardt, D.B., Chen, W.S., Yim, K., van den Elzen, A., Hirn, M.J., Coifman, R.R., Ivanova, N.B., Wolf, G., Krishnaswamy, S.: Visualizing structure and transitions in high-dimensional biological data. *Nature Biotechnology* **37**(12), 1482–1492 (2019). <https://doi.org/10.1038/s41587-019-0336-3>
- [37] Mescheder, L., Nowozin, S., Geiger, A.: The Numerics of GANs. In: *Advances in Neural Information Processing Systems*, vol. 30. Curran Associates, Inc., ??? (2017)
- [38] Arjovsky, M., Bottou, L.: Towards Principled Methods for Training Generative Adversarial Networks. *arXiv* (2017). <https://doi.org/10.48550/arXiv.1701.04862>
- [39] Vis, J.Y., Huisman, A.: Verification and quality control of routine hematology analyzers. *International Journal of Laboratory Hematology* **38**, 100–109 (2016). <https://doi.org/10.1111/ijlh.12503>
- [40] Chen, T., Guestrin, C.: XGBoost: A Scalable Tree Boosting System. In: *Proceedings of the 22nd ACM SIGKDD International Conference on Knowledge Discovery and Data Mining*, pp. 785–794 (2016). <https://doi.org/10.1145/2939672.2939785>

Appendix A Synthetic dataset generation

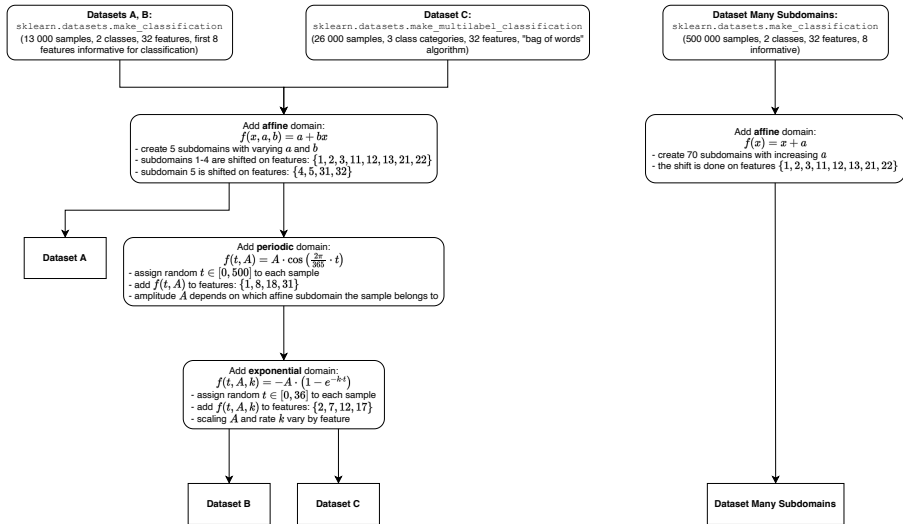


Fig. A1: Overview of the method for generating the synthetic datasets. Each dataset has at least one artificial classification task and domain shift. The added domains are based on simple transformations of some data features.

Appendix B Haematological parameters

The FBC parameters used in this work were taken directly from the corresponding datasets. Tables B1, B2 and B3 list and describe the used HL-FBC and R-FBC parameters. The parameters correspond to standard FBC measurements as well as additional research and clustering parameters recorded by the Sysmex XN-2000 haematology analysers of the INTERVAL and COMPARE trials (see also Section 2).

Table B1: List of used platelet features. (HL-FBC features in bold)

Sysmex Abbreviation	Long Name	Unit
PLT	Platelet count	per nL
PDW	Platelet distribution width	fL
MPV	Mean platelet volume	fL
P-LCR	Platelet - large cell ratio	%
PCT	Plateletcrit	%
IPF	Immature platelet fraction	-
PLT-I	PLT count calculated from the PLT particle size distribution	per nL
PLT-O	PLT count calculated from the RET channel	per nL
PLT-F	PLT count calculated from the PLT-F channel	per nL
H-IPF	High fluorescence immature platelet fraction	-
IPF#	Immature platelet count	per nL

Table B2: List of used red cell features. (HL-FBC features in bold)

Sysmex Abbreviation	Long Name	Unit
RBC	Red blood cell count	per pL
HGB	Haemoglobin concentration	g/dL
HCT	Haematocrit	%
MCV	Mean corpuscular volume	fL
MCH	Mean corpuscular haemoglobin	pg
MCHC	Mean corpuscular haemoglobin concentration	g/dL
RDW-SD	Red cell distribution width (standard deviation)	fL
RDW-CV	Red cell distribution width (coefficient of variation)	%
RET%	Reticulocyte percent	%
RET#	Reticulocyte count	per pL
IRF	Immature reticulocyte fraction	%
LFR	Low fluorescence ratio	%
MFR	Medium fluorescence ratio	%
HFR	High fluorescence ratio	%
RET-He	Reticulocyte haemoglobin equivalent	pg
MicroR	Micro RBC ratio	%
MacroR	Macro RBC ratio	%
RBC-O	RBC count calculated from the RET channel	per pL
RBC-He	Red blood cell haemoglobin equivalent	pg
Delta-He	Delta of the haemoglobin equivalents	pg
RET-Y	Forward-scatter in RET area of RET scattergram	ch
RET-RBC-Y	Forward-scatter in RBC area of RET scattergram	ch
IRF-Y	Forward-scatter in IRF area of RET scattergram	ch
Hypo-He	Hypo-haemoglobinised percentage of red cells	%
Hyper-He	Hyper-haemoglobinised percentage of red cells	%
RPI	Reticulocyte Production Index	-
RET-UPP	Count in the UPP area of the RET scattergram	-
RET-TNC	Count in the TNC area of the RET scattergram	-

Table B3: List of used white cell features. (HL-FBC features in bold)

Sysmex Abbreviation	Long Name	Unit
WBC	White blood cell count	per nL
NEUT#	Neutrophil count	per nL
LYMPH#	Lymphocyte count	per nL
MONO#	Monocyte count	per nL
EO#	Eosinophil count	per nL
BASO#	Basophil count	per nL
NEUT%	Neutrophil percent	%
LYMPH%	Lymphocyte percent	%
MONO%	Monocyte percent	%
EO%	Eosinophil percent	%
BASO%	Basophil percent	%
IG#	Immature granulocyte count	per nL
IG%	Immature granulocyte percent	%
TNC	Total nuclear cell count	per nL
WBC-N	WBC count calculated from WNR channel	per nL
TNC-N	Total nuclear cell count calculated from WNR channel	per nL
BA-N#	Basophil count calculated from the WNR channel	per nL
BA-N%	Basophil percent calculated from the WNR channel	%
WBC-D	WBC count calculated from WDF channel	per nL
TNC-D	Total nuclear cell count calculated from WDF channel	per nL
NEUT#&	Subtraction of IG# from NEUT#	per nL
NEUT%&	Ratio of NEUT#& to WBC	%
LYMP#&	Subtraction of the upper LYMPH AWS from LYMPH#	per nL
LYMP%&	Ratio of LYMP#& to WBC	%
BA-D#	Basophil count calculated from the WDF channel	per nL
BA-D%	Basophil percent calculated from the WDF channel	%
NE-SSC	Lateral scattered light intensity of the NEUT AWS	ch
NE-SFL	Fluorescent light intensity of the NEUT AWS	ch
NE-FSC	Forward-scattered light intensity of the NEUT AWS	ch
LY-X	Lateral-scattered light intensity of the LYMPH AWS	ch
LY-Y	Fluorescent light intensity of the LYMPH AWS	ch
LY-Z	Forward-scattered light intensity of the LYMPH AWS	ch
MO-X	Lateral scattered light intensity of the MONO AWS	ch
MO-Y	Fluorescent light intensity of the MONO AWS	ch
MO-Z	Forward-scattered light intensity of the MONO AWS	ch
NE-WX	Lateral scattered light distribution width of the NEUT AWS	% ₀
NE-WY	Fluorescent light distribution width of the NEUT AWS	% ₀
NE-WZ	Forward-scattered light distribution width of the NEUT AWS	% ₀
LY-WX	Lateral scattered light distribution width of the LYMPH AWS	% ₀
LY-WY	Fluorescent light distribution width of the LYMPH AWS	% ₀
LY-WZ	Forward-scattered light distribution width of the LYMPH AWS	% ₀
MO-WX	Lateral scattered light distribution width of the MONO AWS	% ₀
MO-WY	Fluorescent light distribution width of the MONO AWS	% ₀
MO-WZ	Forward-scattered light distribution width of the MONO AWS	% ₀

AWS: area on the white cell differential fluorescence scattergram

Appendix C Preparation of FBC data from the INTERVAL and COMPARE trials

The pre-filtering on the available rich FBC data from the INTERVAL and COMPARE trials is outlined in Figure C2. The distributions of the various task and domain labels in the pre-filtered dataset are displayed in Figure C3.

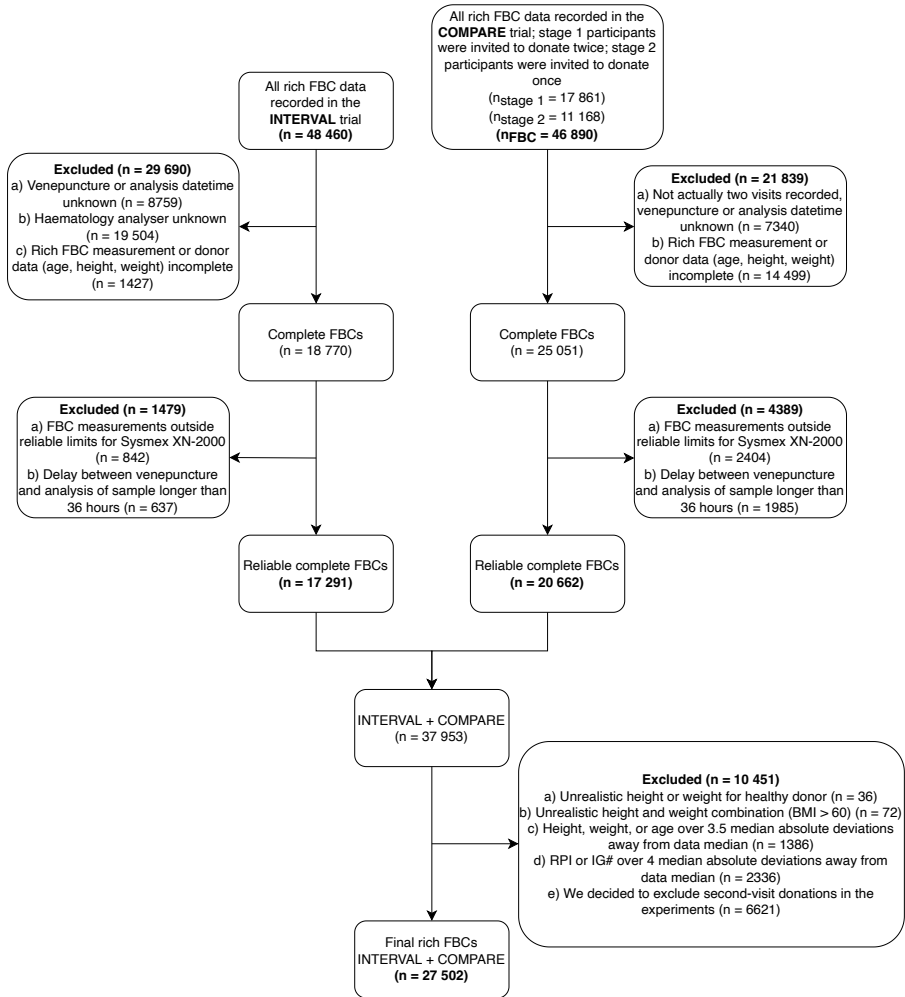


Fig. C2: Flowchart of the pre-filtering of the available rich FBC data from the INTERVAL and COMPARE trials for the experiments in this paper. We used Vis & Huisman’s [39] suggested reliability limits for FBC quality control as exclusion criteria. Similarly, we only considered samples with a subject height within 1 m to 2.2 m, subject weight within 45 kg to 200 kg, and subject BMI less than 60. We only used first-visit donations per donor.

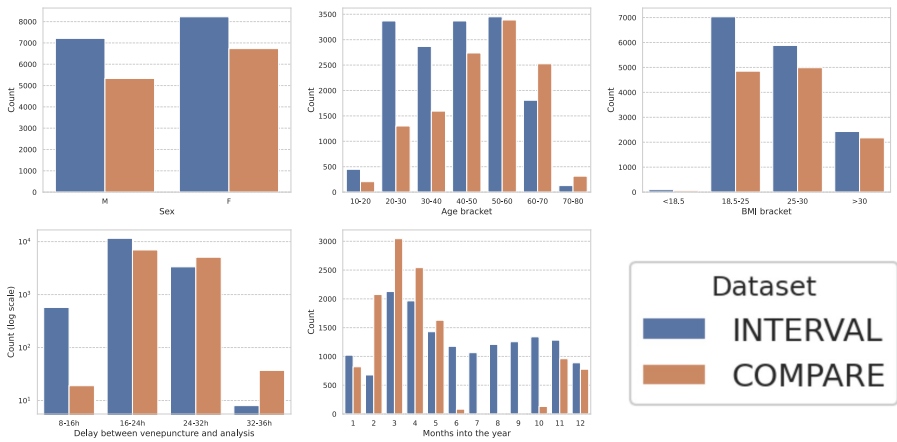


Fig. C3: Histogram plots of the various task and domain label distributions in the pre-filtered rich FBC data from the INTERVAL and COMPARE trials, coloured by blood donor study of origin.

Appendix D Preparation of FBC data from the Cambridge University Hospitals dataset

The pre-filtering on the available high-level FBC data from the CUH dataset is outlined in Figure D4. The distributions of the various task and domain labels in the pre-filtered dataset are displayed in Figure D5.

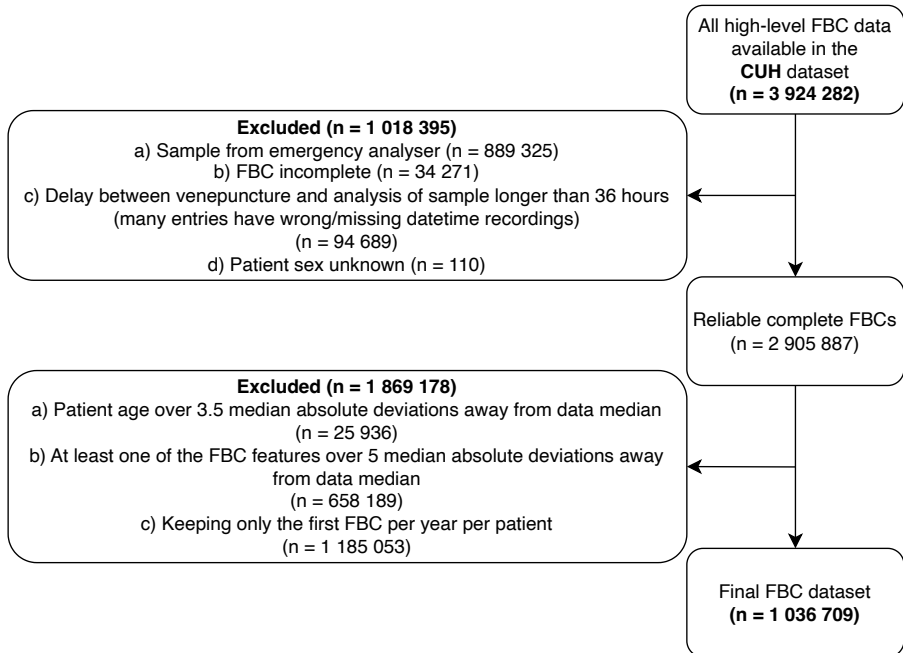


Fig. D4: Flowchart of the pre-filtering of the available high-level FBC data from the CUH dataset for the experiments in this paper. We chose to only include the first FBC per year per patient so as to not create a large bias towards very ill patients who would have many more FBCs in a short time interval than comparatively healthier ones.

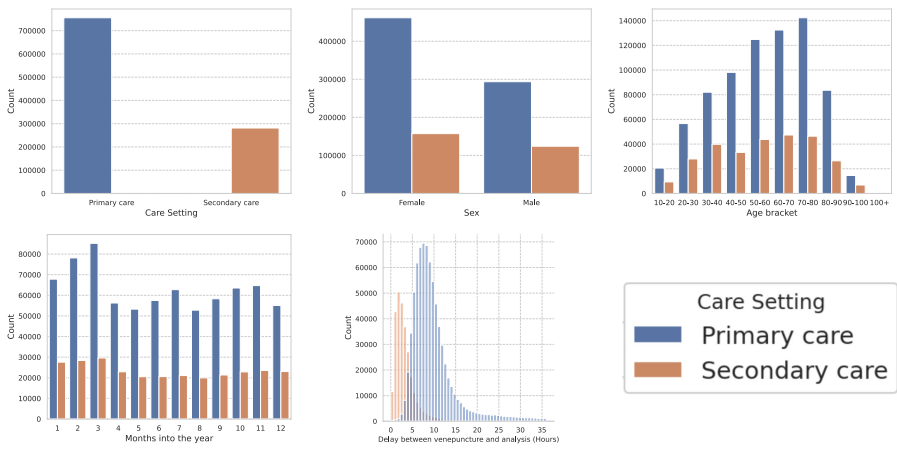


Fig. D5: Histogram plots of the various task and domain label distributions in the pre-filtered high-level FBC data from the CUH dataset, coloured by patient care setting.

Appendix E Supplementary: Dis-AE experiment results

E.1 Synthetic datasets experiments

The quantitative performance for both task and domain objectives was measured using the classification accuracy of an XGBoost [40] model and the variation V^{sup} on various representations of the data. Results for datasets A, B and C are displayed in Tables E4 and E5.

It is visible that instance 5, being different from the other ones on different features, showed a drop in performance in all representations. Particularly the Dis-AE model seems to have difficulties as it is only trained to ignore differences in the features where instances 1 and 2 differ. This gives an early indication that the robustness of the model depends heavily on the domain diversity of its source data.

Model	Task	Classification Accuracy			
		Source	Target		
Raw data	Task 1	Inst. 1&2	Inst. 3	Inst. 4	Inst. 5
Vanilla AE	Task 1	97 %	97 %	96 %	72 %
Dis-AE	Task 1	98 %	98 %	97 %	53 %

(a) Dataset A

Model	Task	Classification Accuracy			
		Source	Target		
Raw data	Task 1	Inst. 1&2	Inst. 3	Inst. 4	Inst. 5
Vanilla AE	Task 1	97 %	97 %	96 %	71 %
Dis-AE	Task 1	96 %	94 %	76 %	51 %
Dis-AE	Task 1	98 %	97 %	96 %	53 %

(b) Dataset B

Model	Task	Classification Accuracy			
		Source	Target		
Raw data	Task 1	Inst. 1&2	Inst. 3	Inst. 4	Inst. 5
	Task 2	83 %	80 %	75 %	75 %
	Task 3	81 %	79 %	65 %	76 %
Vanilla AE	Task 1	74 %	68 %	66 %	67 %
	Task 2	68 %	69 %	68 %	64 %
	Task 3	73 %	73 %	73 %	68 %
Dis-AE	Task 1	67 %	63 %	67 %	63 %
	Task 2	75 %	76 %	74 %	57 %
	Task 3	77 %	78 %	76 %	70 %
Dis-AE	Task 3	70 %	69 %	67 %	62 %

(c) Dataset C

Table E4: Accuracy of an XGBoost [40] classifier on various representations of the synthetic datasets. The representations are the raw datasets, the embedding of a regular autoencoder and the embedding of our Dis-AE model. Target data performance is given for a classifier only trained on the full source data.

Model	Variation V^{sup}			
	Within source	Source + target		
	Inst. 1&2	Inst. 3	Inst. 4	Inst. 5
Raw data	3.3	3.9	11.5	11.4
Vanilla AE	3.6	4.0	9.8	17.4
Dis-AE	0.01	0.04	0.1	8.5

(a) Dataset A

Model	Variation V^{sup}			
	Within source	Source + target		
	Inst. 1&2	Inst. 3	Inst. 4	Inst. 5
Raw data	10.4	10.4	12.2	11.8
Vanilla AE	7.0	6.9	10.0	12.2
Dis-AE	0.1	0.1	0.3	8.4

(b) Dataset B

Model	Variation V^{sup}			
	Within source	Source + target		
	Inst. 1&2	Inst. 3	Inst. 4	Inst. 5
Raw data	10.4	10.4	12.2	11.8
Vanilla AE	6.4	6.5	6.5	5.9
Dis-AE	0.7	0.8	3.8	2.4

(c) Dataset C

Table E5: Variation V^{sup} of various representations of the synthetic datasets. The representations are the raw datasets, the embedding of a regular autoencoder and the embedding of our Dis-AE model. V^{sup} gives a measure of the maximum domain shift in each representation. (We used ρ_{W_2} for the calculation of V^{sup} as the domain shift in the synthetic datasets is so large that ρ_{JSD} always returns 1 on the raw data and vanilla AE latent space.)

E.2 Rich FBC data experiments

This appendix section displays further more detailed results on the per-class accuracies for the rich FBC data experiments. It is worth noting that all classes which have 0% classification accuracy across the board were only represented by very few data points (1-10).

Sex	Representation	Class Accuracy	
		Source INTERVAL	Target COMPARE
Male	Raw data	85 %	76 %
	Vanilla AE	83 %	74 %
	Dis-AE	83 %	70 %
Female	Raw data	89 %	93 %
	Vanilla AE	87 %	92 %
	Dis-AE	87 %	93 %

BMI	Representation	Class Accuracy	
		Source INTERVAL	Target COMPARE
≤ 18.5	Raw data	0 %	0 %
	Vanilla AE	0 %	0 %
	Dis-AE	0 %	0 %
18.5-25	Raw data	64 %	72 %
	Vanilla AE	63 %	69 %
	Dis-AE	62 %	67 %
25-30	Raw data	53 %	41 %
	Vanilla AE	51 %	45 %
	Dis-AE	51 %	46 %
≥ 30	Raw data	24 %	22 %
	Vanilla AE	21 %	18 %
	Dis-AE	20 %	21 %

Table E6: Performance on rich FBC datasets (part 1/2).

Tasks: sex, age bracket, BMI range

Domains: haem. analyser, delay between venepuncture and analysis, time of year

Age	Representation	Class Accuracy	
		Source INTERVAL	Target COMPARE
≤ 20	Raw data	1 %	1 %
	Vanilla AE	2 %	1 %
	Dis-AE	0 %	1 %
20-30	Raw data	35 %	52 %
	Vanilla AE	32 %	53 %
	Dis-AE	25 %	42 %
30-40	Raw data	17 %	17 %
	Vanilla AE	15 %	17 %
	Dis-AE	14 %	16 %
40-50	Raw data	30 %	25 %
	Vanilla AE	29 %	21 %
	Dis-AE	28 %	22 %
50-60	Raw data	45 %	31 %
	Vanilla AE	45 %	28 %
	Dis-AE	45 %	34 %
60-70	Raw data	30 %	20 %
	Vanilla AE	27 %	20 %
	Dis-AE	24 %	18 %
≥ 70	Raw data	1 %	0 %
	Vanilla AE	0 %	0 %
	Dis-AE	0 %	0 %

Table E7: Performance on rich FBC datasets (part 2/2).

Tasks: sex, age bracket, BMI range

Domains: haem. analyser, delay between venepuncture and analysis, time of year

E.3 Cambridge University Hospitals data experiments

This appendix section includes experiment results from the CUH dataset experiments. The results are presented similarly to those of the other datasets and are included for sake of completeness. Interestingly, comparing Table 1 and Table E8, we see that the Dis-AE model struggles to achieve good generalisation and classification performance on the care setting task and the sample age domain. Indeed we found that sample age distributions between primary and secondary care patients barely overlapped and hence this task and domain are highly correlated. In trying to remove domain information for sample age the model inadvertently dampened the classification performance of the care setting task. Optimising this task and domain performance is non-trivial and requires careful tuning of the α and λ hyperparameters in the model loss function.

Representation	Domain	Variation V^{sup}	
		Within source (2120I 2 & 3)	Source and target (All analysers)
(A) Raw data	Analysers	0.28	0.56
	Sample age	0.64	0.49
	Time of year	0.19	0.83
(B) Vanilla AE	Analysers	0.15	0.39
	Sample age	0.78	0.53
	Time of year	0.19	0.68
(C) Dis-AE	Analysers	0.04	0.37
	Sample age	0.64	0.46
	Time of year	0.17	0.71

Table E8: Variation of HL-FBC data from the Cambridge University Hospitals patient dataset in different representations. The three representations are: (A) the unmodified data, (B) the latent space of a vanilla AE and (C) the latent space of the Dis-AE model. The variation V^{sup} , calculated using ρ_{JSD} , is shown per domain to show each covariate’s contribution to the data’s domain shift.

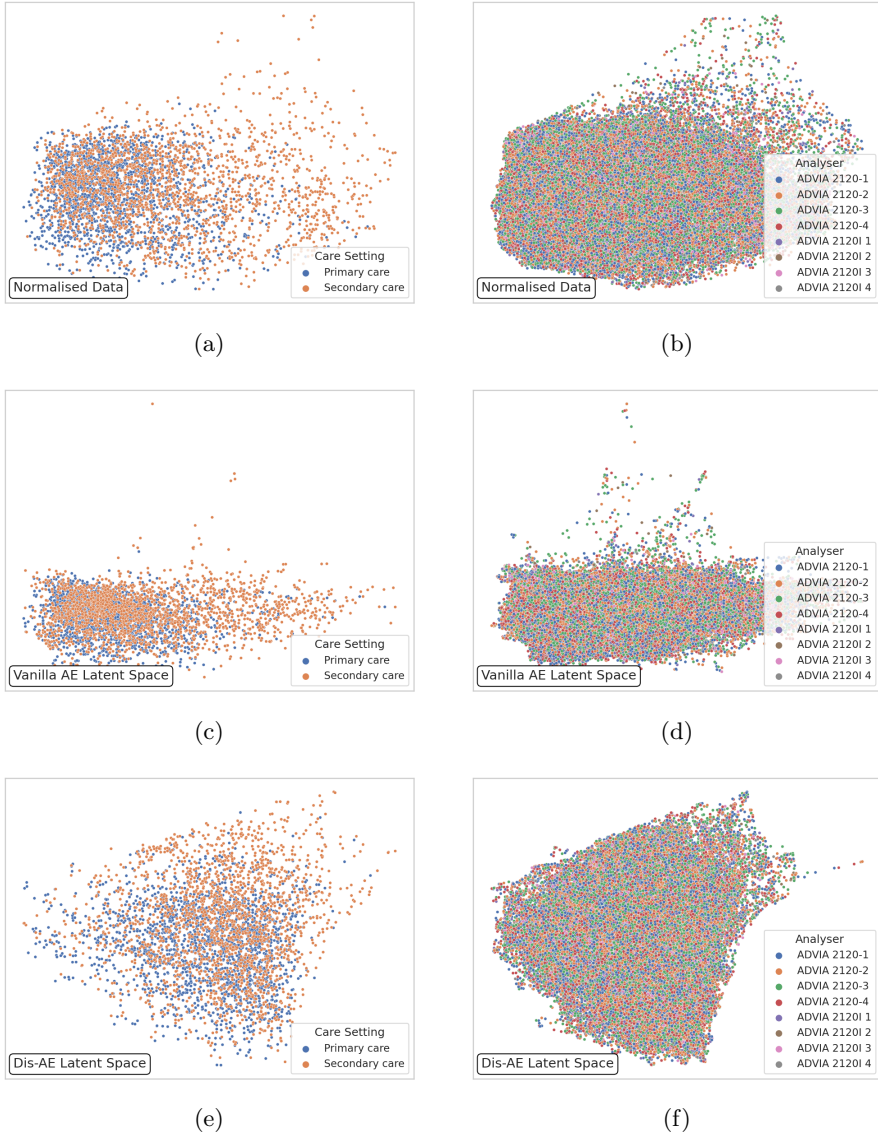


Fig. E6: HL-FBC hospital patient data PHATE [36] visualisation of normalised raw data (row 1) and latent spaces of a vanilla AE (row 2) and the Dis-AE model (row 3). The images in the left column are coloured by patient care setting (example task), while those in the right column are coloured by haematology analyser (example domain). The machine learning models were only trained on data measured on the ADVIA 2120I 2 and ADVIA 2120I 3 analysers. In all plots, 2000 points per class were randomly selected from the calculated PHATE representation.

Sex	Representation	Class Accuracy	
		Source 2120I 2 & 3	Target (all other analysers)
Male	Raw data	64 %	65 %
	Vanilla AE	63 %	64 %
	Dis-AE	63 %	65 %
Female	Raw data	83 %	83 %
	Vanilla AE	83 %	83 %
	Dis-AE	83 %	83 %

Care Setting	Representation	Class Accuracy	
		Source 2120I 2 & 3	Target (all other analysers)
Primary	Raw data	90 %	92 %
	Vanilla AE	90 %	91 %
	Dis-AE	90 %	91 %
Secondary	Raw data	53 %	46 %
	Vanilla AE	52 %	46 %
	Dis-AE	41 %	38 %

Table E9: Performance on HL-FBC dataset (part 1/2).

Tasks: sex, age bracket, care setting

Domains: haem. analyser, delay between venepuncture and analysis, time of year

Age	Representation	Class Accuracy	
		Source 2120I 2 & 3	Target (all other analysers)
≤ 20	Raw data	3 %	2 %
	Vanilla AE	3 %	2 %
	Dis-AE	3 %	2 %
20-30	Raw data	9 %	5 %
	Vanilla AE	9 %	5 %
	Dis-AE	7 %	5 %
30-40	Raw data	28 %	21 %
	Vanilla AE	27 %	20 %
	Dis-AE	26 %	21 %
40-50	Raw data	11 %	10 %
	Vanilla AE	11 %	9 %
	Dis-AE	10 %	9 %
50-60	Raw data	28 %	30 %
	Vanilla AE	27 %	30 %
	Dis-AE	30 %	30 %
60-70	Raw data	19 %	21 %
	Vanilla AE	18 %	21 %
	Dis-AE	19 %	20 %
70-80	Raw data	43 %	42 %
	Vanilla AE	43 %	41 %
	Dis-AE	44 %	42 %
80-90	Raw data	27 %	30 %
	Vanilla AE	27 %	30 %
	Dis-AE	27 %	29 %
90-100	Raw data	1 %	1 %
	Vanilla AE	1 %	1 %
	Dis-AE	1 %	1 %
≥ 100	Raw data	0 %	0 %
	Vanilla AE	0 %	0 %
	Dis-AE	0 %	0 %

Table E10: Performance on HL-FBC dataset (part 2/2).

Tasks: sex, age bracket, care setting

Domains: haem. analyser, delay between venepuncture and analysis, time of year